Observing the Sun: from start to finish.

PhD dissertation by

Pablo Santamarina Guerrero

Instituto de Astrofísica de Andalucia (IAA-CSIC)

Programa de Doctorado en Física y Matemáticas (FisyMat)
Universidad de Granada

A thesis submitted in fulfillment
of the requirements of the degree of
Doctor of Philosophy

June 25, 2024

PhD thesis supervised by

Dr. David Orozco Suárez
Dr. Julián Blanco Rodríguez

Acknowledgements

Agradecimientos

Resumen

Resumen de la tesis

Summary

Summary of the thesis

CONTENTS

CHALLENGES IN DATA REDUCTION. ETALON CAVITY MAP.

INTRO. https://link.springer.com/article/10.1007/s10509-023-04212-3

1.1 One device, two configurations.

We established in section **??** that the observed intensity distribution at the coordinates ξ, η of the focal plane of any etalon-based instrument tuned to a wavelength λ_s obeys the following expression (Bailén et al., 2019):

$$I\left(\xi,\eta;\lambda_s\right) = g(\xi,\eta) \int_0^\infty T(\lambda) \iint O\left(\xi_0,\eta_0;\lambda\right) \mathcal{S}\left(\xi_0,\eta_0;\xi,\eta;\lambda-\lambda_s\right) \mathrm{d}\xi_0\,\mathrm{d}\eta_0\mathrm{d}\lambda, \quad (1.1)$$

where $T(\lambda)$ accounts for the presence of an order-sorting pre-filter, $O\left(\xi_0,\eta_0;\lambda\right)$ represents the brightness distribution of the observed object at the point $\left(\xi_0,\eta_0\right)$, $S\left(\xi_0,\eta_0;\xi,\eta;\lambda-\lambda_s\right)$ accounts for the imaging response of the instrument when tuned at the wavelength λ_s, and $g(\xi,\eta)$ represents a spatial gain factor that accounts for wavelength independent pixel-to-pixel intensity fluctuations ocurring in the focal plane due to differences in the detectors' sensitivity.

The imaging response of the instrument coincides with the PSF of the instrument when the optical response is invariant against translations. In such a case, we can substitute the last two integrals by the convolution operator, but this is not strictly true in etalon-based instruments, where the response varies pixel to pixel either because of etalon irregularities or because of variations in the illumination across its clear aperture.

Deriving S typically requires determining the electric field of the polychromatic wave in the image plane. According to Bailén et al. (2019), this field can be calculated by summing all the electric fields ($E^{(t)}$) across the pupil, such that the eletric field at any point (ξ,η) of the image plane follows the expression:
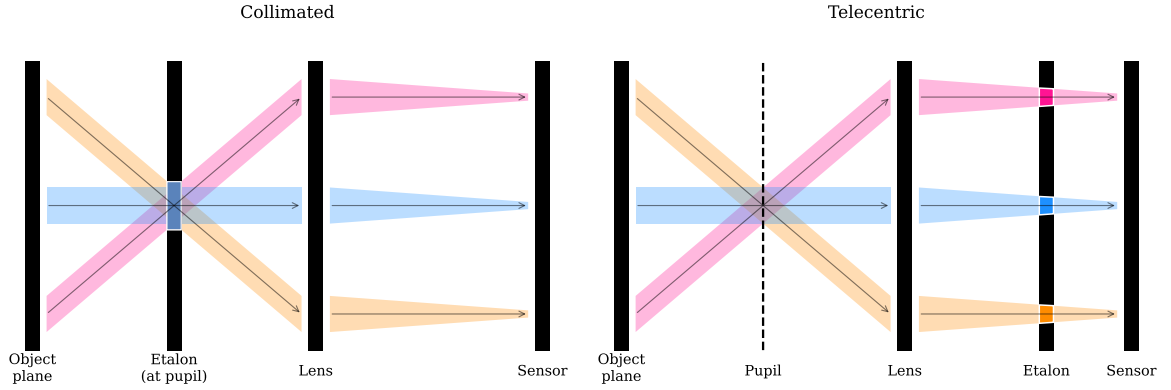
Figure 1.1 Schematic representation of the two optical setups of an FPI, collimated (left) and telecentric (right). The different colors represent distinct light rays originating from various points on the object plane. The white boxes in the etalon highlight the sections that are traversed by the light rays.

$$E_{im}^{(t)}(\xi, \eta) = \frac{1}{\pi R_{pup}^2} \int \int_{pupil} E^{(t)}(x, y) e^{-ik(\xi x/f + \eta y/f) dx dy}, \tag{1.2}$$

where (x, y) are the coordinates in the pupil, f stands for the focal length, and R_{pup} is the radius of the pupil. It can also be shown that the vector electric fields transmitted by the etalon can be expressed as:

$$E^{(t)}(\xi, \eta) = \frac{\sqrt{\tau}}{1 - R} \frac{e^{i\delta/2} - R e^{-i\delta/2}}{1 + F \sin^2(\delta/2)} E^{(i)}, \tag{1.3}$$

where τ is the transmission factor for normal incidence, R stands for the reflectivity of the etalon mirrors, F is a factor defined as $F \equiv 4R(1 - R)^{-2}$, $E^{(i)}$ are the incident electric fields, and δ stands for the phase differences between the transmitted and incident rays.

The transmission profile of the etalon (S) is defined as the average ratio between the transmitted and incident intensities, calculated from the complex conjugate of the corresponding electric fields. The shape of δ varies depending on the illumination setup of the etalon, whether collimated or telecentric. Consequently, each configuration has unique solutions and characteristics and is differently affected by inhomogeneities (defects) in the etalon's properties.

1.1.1 Collimated configuration

Collimated mounts are characterized by having the etalon located at the pupil plane and therefore receive a collimated beam from each point of the observed object. As illustrated in the schematic on the left side of fig. 1.1, light from any point on the object will fall on the same area of the etalon. Consequently, any local defects on the etalon crystals or on the plates' parallelism is averaged all over the clear aperture, thus making the optical quality

constant along the FoV. However, the angle of incidence of the light beam varies along the FoV, thus shifting the spectral transmission profile.

Analytical solutions of equation (1.2) are imposible to obtain if δ has a dependence on the pupil coordinates, as is the case of collimated etalons with a presence of local defects. In that case, the transmssion profile of the etalon has to be evaluated numerically.

However, in order to study the spectral behavior of the transmission profile, we can, as a first-order approximation, disregard the spatial PSF and focus solely on the spectral transmission profile (ψ). Under this assumption, the phase difference between the incident and transmitted rays of an ideal collimated etalon can be expressed as:

$$\delta(\xi, \eta, \lambda) = \frac{4\pi}{\lambda} nd \cos(\theta(\xi, \eta)), \tag{1.4}$$

where n stands for the refractive indx of the etalon cavity, d is the distance between the mirrors and θ is the angle of incidence. In such a case, it can be shown that the spectral transmission profile follows the expression:

$$\psi\left(\xi, \eta, \lambda\right) = \frac{\tau}{1 + F \sin^2(\delta(\xi, \eta, \lambda)/2)}. \tag{1.5}$$

The spectral behaviour of the transmission profile, such as the spectral position of the resonance peaks and the distance between them (the free spectral range), is encoded in the parameter δ, which is a function of the refractive index of the etalon cavity, the distance between mirrors, and the angle of the incident beam. The reflectivity R of the mirrors determines the width of the resonance peaks through the parameter F, $F \equiv 4R(1 - R)^{-2}$.

Local defects in the collimated configuration are averaged out, which means that d and n respectively represent the mean values of the thickness and refractive index across the clear aperture of the FPI, and thus remain constant for every pixel. Yet, they produce a broadening of the transmission profile and worsen the optical quality of the instrument. However, the spatial dependence of ψ naturally arises from θ, which vcaries from pixel to pixel.

Assessing the spatial PSF of the FPI is more challenging, as it can only be determined analytically for monochromatic light and in the absence of defects. We will not delve into the equations for this specific scenario as it lies beyond the scope of this thesis. However, interested readers are referred to the work of Bailén et al. (2019), where this topic is extensively discussed.

1.1.2 Telecentric configuration

In the telecentric configuration, the etalon is placed very close to an intermediate focal plane, while the pupil is focused at infinity. As shown in the sketch on the right side of fig. 1.1, in this setup, the etalon is illuminated by cones of rays that are parallel to each other, thus passing through different sections of the interferometer. Local inhomogeneities (defects or cavities) on the etalon produce differences in the transmission profile across the

FoV, which are directly mapped into the image plane. This means that the optical response and the transmission profile shift locally on the image sensor.

In telecentric configurations, δ always depends on the coordinates of the pupil, even in the absence of defects, since each point in the etaon sees a cone of rays coming from different parts of the pupil. Thus, as stated before, solutions to equation (1.2) are to be found numerically. Nonetheless, if we neglect the spatial PSF once again, we can derive an analytical expression for an ideal telecentric etalon, where all light cones impact perpendicularly.

After some messy algebra and clever variable changes, one can recast eq. (1.2) in terms of the radial coordinates of the pupil and anallytically solve the equations. The resulting spectral transmission profile of an ideal telecentric etalon is given by (Bailén et al., 2021):

$$\Psi\left(\xi, \eta, \lambda\right) = \Re\left[E(a\left(\xi, \eta, \lambda\right), b\left(\xi, \eta, \lambda\right))\right]^2 + \Im\left[E(a\left(\xi, \eta, \lambda\right), b\left(\xi, \eta, \lambda\right))\right]^2, \quad (1.6)$$

with $E(a\left(\xi, \eta, \lambda\right), b\left(\xi, \eta\right))$ being:

$$E(a\left(\xi, \eta, \lambda\right), b\left(\xi, \eta\right)) = 2\sqrt{\tau}\left\{\frac{1}{\alpha_1}\left[\arctan(\gamma_1) - \arctan(\gamma_2)\right] + \right.$$

$$\left. i\frac{1+R}{1-R}\frac{1}{\alpha_2}\left[\ln\left(\frac{(1+\gamma_3)^2 + \gamma_4^2}{(1-\gamma_3)^2 + \gamma_4^2}\right) - \ln\left(\frac{(1+\gamma_3)^2 + \gamma_5^2}{(1-\gamma_3)^2 + \gamma_5^2}\right)\right]\right\}, \quad (1.7)$$

where, the auxiliary functions are defined as:

$$a\left(\xi, \eta, \lambda\right) \equiv \frac{2\pi}{\lambda}n\left(\xi, \eta\right)d\left(\xi, \eta\right),$$

$$b\left(\xi, \eta\right) \equiv \frac{1}{8n\left(\xi, \eta\right)^2 (f\#)^2},$$

$$\alpha_1 \equiv 2ab\sqrt{F},$$

$$\alpha_2 \equiv 2\alpha_1\sqrt{F+1},$$

$$\gamma_1 \equiv \sqrt{F}\sin a,$$

$$\gamma_2 \equiv \sqrt{F}\sin(a[1-b]),$$

$$\gamma_3 \equiv \sqrt{\frac{F}{F+1}},$$

$$\gamma_4 \equiv \frac{\tan\left(a/2[1-b]\right)}{\sqrt{F+1}},$$

$$\gamma_5 \equiv \frac{\tan(a/2)}{\sqrt{F+1}}.$$

$$(1.8)$$

The parameter a has the same role as δ for the collimated case. However, the dependence on the image plane coordinates in this case is caused by potential variations in n and/or d, as each light beam traverses different sections of the etalon. These variations

constitute the "cavity map" of a telecentric etalon and must always be taken into account during data reduction processes.

The parameter b accounts for the contribution of the focal ratio, $f\#$, and has an impact on the spectral resolution and the apodization of the pupil as seen from the etalon (Beckers, 1998). Thus, the resolution is now affected by both F and $f\#$, through the parameters a and b.

1.1.2.1   Telecentric imperfect configuration

The equations shown in Sect. 1.1.2 are valid whenever the incident cone of rays is perpendicular to the etalon mirrors. We refer to this situation hereinafter as "perfect telecentrism". However, real instruments are likely to present deviations from such an ideal case. These deviations can be caused by an intentional tilt of the etalon to suppress ghost images on the detector (Scharmer, 2006), by an accidental tilted angle of incidence caused by deviations from the ideal paraxial propagation of rays within the instrument, or simply because of misalignment of the optical components. In the three cases, the incident cone of rays is no longer perpendicular to the etalon, and hence, we consider these scenarios to have imperfections in the telecentrism degree. One important consequence of the loss of telecentrism is an asymmetrization of the transmission profile that must be accounted for when modeling the instrument response.

The transmission profile in this case is influenced by the angle of incidence of the chief ray at each point of the clear aperture of the etalon, in addition to the parameters mentioned in the previous sections. Unfortunately, the equations for the transmission profile in these configurations are much more complicated than in the ideal case, and can no longer be anallytically solved. We must revisit equation (1.2) and solve the integrals numerically. We highlight the distinction between perfect and imperfect telecentrism because any real instrument will exhibit such deviations. This difference is especially significant in the subsequent sections, where the impact of asymmetries on solar observations is analyzed.

Figure 1.2 shows the transmission profile corresponding to the three different scenarios we have considered: collimated illumination of the etalon, perfect telecentrism, and imperfect telecentrism. The etalon parameters have been selected to coincide with those of SO/PHI's etalon. In both the collimated and perfect telecentric configurations, a normal incidence ($\theta = 0$) scenario is shown, whereas in the imperfect telecentric case, we assumed an angle of incidence of the chief ray, Θ, of $0.3°$. The parameter a has been adjusted slightly in order to tune the transmission profile at λ_0.

We observed that the telecentric configurations achieve lower peak transmissions than the collimated case. In addition, the telecentric profiles are wider due to the different incidence angles across the illuminating cone of rays. Such a broadening increases with decreasing f-ratios. Lastly, non-normal incidence of the chief ray in the telecentric configuration further widens and shifts (~ 4 mÅ for $\Theta = 0.3°$) the profile, making it asymmetrical.
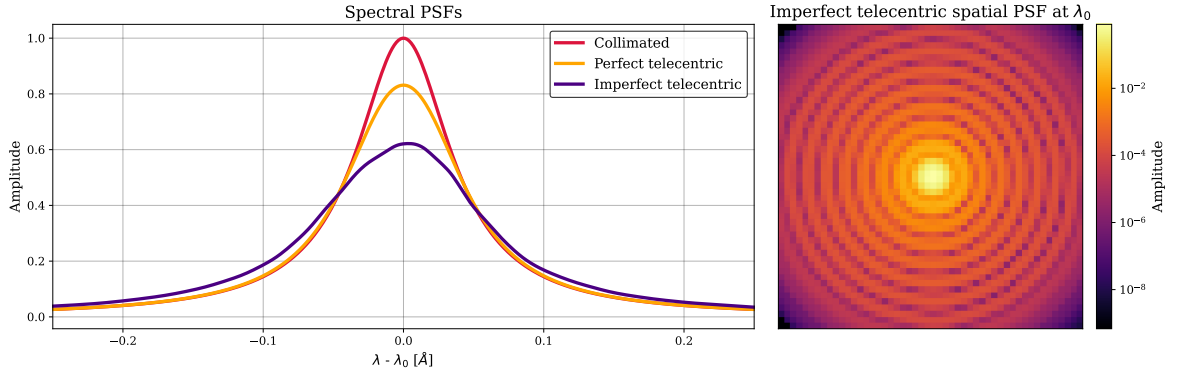
Figure 1.2 *Left*: central peak of the etalon's spectral transmission profile for the three different configurations. *Right*: Spatial PSF of the imperfect telecentric etalon at λ_0. The parameters of the etalon are $R = 0.92$, $n = 2.29$, $d = 251\,\mu\text{m}$, $f\# = 56$, $\theta = 0°$ (collimated and perfect telecentric), and $\Theta = 0.3°$ (imperfect telecentric).

1.2 Fitting algorithm

1.2.1 Initial approximations

The intensity distribution observed at the focal plane of any etalon-based instrument tuned to a wavelength λ_s obeys the following expression (Bailén et al., 2019):

As a first approximation, we assumed a spatial dependence of the imaging response in the form of a Dirac delta in order to simplify the equations. If we let the imaging response follow the expression

$$S\left(\xi_0, \eta_0; \xi, \eta; \lambda - \lambda_s\right) = \delta(\xi_0 - \xi, \eta_0 - \eta)\Psi(\xi, \eta, \lambda - \lambda_s), \tag{1.9}$$

where $\Psi\left(\xi, \eta; \lambda - \lambda_0\right)$ is the transmission profile of the etalon, Eq. (**??**) can be simplified as

$$I\left(\xi, \eta; \lambda_s\right) = g(\xi, \eta) \int_0^\infty T(\lambda)O\left(\xi, \eta; \lambda\right) \Psi\left(\xi, \eta; \lambda - \lambda_s\right) \mathrm{d}\lambda. \tag{1.10}$$

The transmission profile has a spatial dependence across the image that arises naturally from the different illumination of the etalon across the FoV in the collimated configuration and from the direct mapping of the local inhomogeneities into the detector in the telecentric configuration.

Although, in practice, it is not often possible to fully characterize the pre-filter, we assumed it has a rectangular shape centered at the wavelength of the observed spectral line (λ_0) and a width of $2\Delta\lambda$ such that only one order of the etalon passes through. We note that including a different shape of the pre-filter in the current model is straightforward, provided it can be modeled analytically or even numerically. With this consideration, equation (1.10) can be written as follows:

$$I(\xi, \eta; \lambda_s) = g(\xi, \eta) \int_{\lambda_0 - \Delta\lambda}^{\lambda_0 + \Delta\lambda} O(\xi, \eta; \lambda)\Psi(\xi, \eta; \lambda - \lambda_s)\mathrm{d}\lambda. \tag{1.11}$$

The explicit shape of Ψ is different depending on the optical configuration of the instrument, that is, collimated or telecentric.

1.2.2　Simulated observations

All the instruments built around the use of an etalon as a wavelength filtering element operate in a very similar way. They scan a spectral line by tuning the etalon (by changing the distance between mirrors and/or modifying the refractive index) to a desired number of wavelengths along the spectral line. At each spectral position, the solar scene is recorded. The measured intensity is approximately given by Eq. (1.11), with the etalon's transmission profile centered at the desired wavelength.

We carried out a series of simulations of a spectral line observation in different conditions. We used the Kitt Peak FTS-Spectral-Atlas as the reference (Brault & Neckel, 1987) and, specifically, the Fe I spectral line at 6173.3 Å. Each observation was composed of N_λ wavelengths, where the measured intensity was recorded. At every wavelength λ_s, the corresponding transmission profile of the etalon Ψ^{λ_s} was computed, and the "observed" intensity $I_{\mathrm{obs},i}^{\lambda_s}$ corresponding to a specific spatial location (ξ, η), represented hereinafter by the pixel i, was calculated using Eq. (1.11). Additionally, we took into account the presence of additive Gaussian noise. This noise does not necessarily respond to any parameter fluctuation within our analytical expressions or photon noise but comes from any unexpected variations that may not have been modeled in the theoretical scheme.

Additionally, we included the presence of defects arising from irregularities or inhomogeneities on either the cavity thickness d, the refractive index n, or from deviations of the angle of incidence θ. In order to simulate this, we introduced a relative perturbation Δa into the etalon equation that accounts for any local deviation of the value of a with respect to its nominal value. This parameter changes from pixel to pixel differently for the collimated and telecentric configurations. In the former, the profile shifts across the FoV only because of the different incidence angles of the light beam on the etalon. In the latter, local variations of n and/or d are mapped directly onto the detector. We also note that variations in the incidence angle must be considered as well when the degree of telecentrism varies along the detector. Analytically, the parameter a at each i-th pixel is given by $a_i' = a \Delta a_i$, where $a = (2\pi/\lambda) n d \cos \theta$ is constant along the FoV.

We let $n_i^{\lambda_s}$ be the noise contribution at the i-th pixel and wavelength λ_s. Thus, the observed intensity at that pixel when the etalon is tuned at λ_s, $I_{\mathrm{obs},i}^{\lambda_s}$ is given by

$$I_{\mathrm{obs},i}^{\lambda_s} = g_i \frac{\int_{\lambda_0-\Delta\lambda}^{\lambda_0+\Delta\lambda} O(\lambda)\Psi^{\lambda_s}(\lambda, \Delta a_i)d\lambda}{\int_{\lambda_0-\Delta\lambda}^{\lambda_0+\Delta\lambda} O(\lambda)\Psi^{\lambda_c}(\lambda, \Delta a_i)d\lambda} + n_i^{\lambda_s}, \tag{1.12}$$

with λ_c being the continuum wavelength. From a practical point of view, the integration limits are set in such a way that only a single resonance (or order) of the etalon is included with the limits, thus, acting akin to the sorting pre-filter commented on previously. We note that the denominator strictly corresponds to the intensity at the continuum of the line
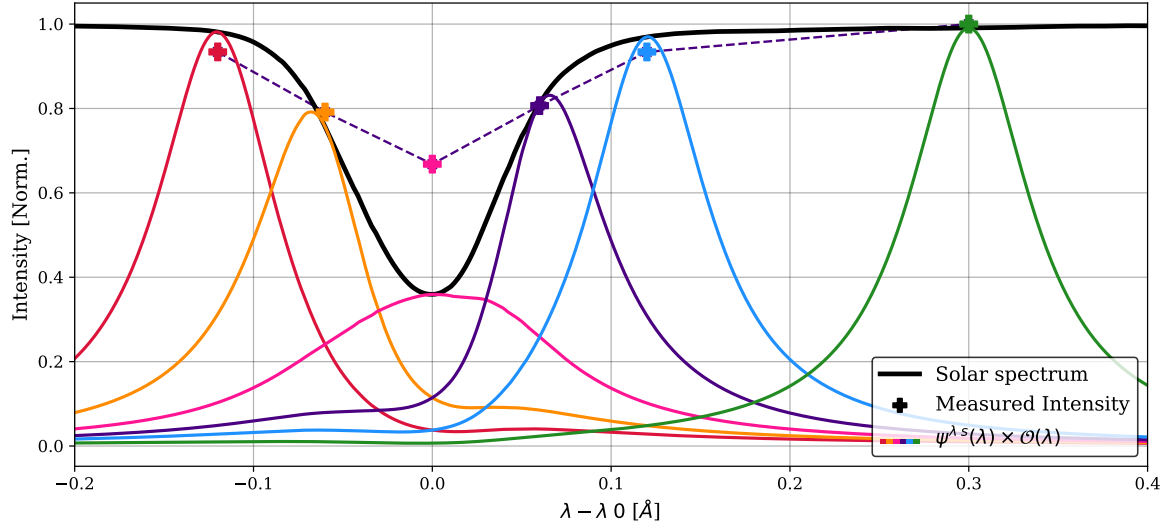
Figure 1.3 Simulated observation of the Fe I spectral line ($\lambda_0 = 6173.3$Å) using a collimated mount and a total of $N_\lambda = 6$ wavelengths that have been equally distributed along the spectral line, with the exception of the continuum measurement (light blue), which is selected at 300 mÅ from the blue of the line core. The measured intensity is the result of computing the value given by Eq. 1.12 at each wavelength and with $g = 1$.

in the absence of the transmission profile or if the continuum wavelength is far enough from the spectral line. In any other case, the transmission should be taken into account as well to normalize the observations to the local continuum, which is necessary since we work with relative measurements. An example of a spectral line measurement is displayed in Fig. 1.3.

For both the collimated and telecentric configurations, we modeled etalon and gain imperfections over a 100×100 px^2 image. Pixel-to-pixel variations in the sensor efficiency were modeled following a random spatial distribution, as shown in Fig. 1.4 (top panel). Additionally, we included a set of pixels with very low gain values, which represent a group of dead pixels or dust grains.

We modeled the etalon defects as changes in Δa in such a way that the maximum displacement reaches 3 pm. The spatial distribution of the values of Δa follows an increasing radial distribution, as shown in Fig. 1.4 (bottom panel). Such a spatial distribution coincides with the expected one in collimated etalons due to the change in the incidence angle across the FoV. Telecentric mounts do not exhibit a spatial distribution of their defects such as this, but using the same spatial distribution in the two cases allowed us to compare the performance of the method for both setups in a systematic way. Since Δa accounts for relative perturbations, it is by definition an adimensional parameter. However, to grant it a physical meaning, we express the values of Δa in Å, representing the associated shift of the transmission profile with respect to the original position determined by a.
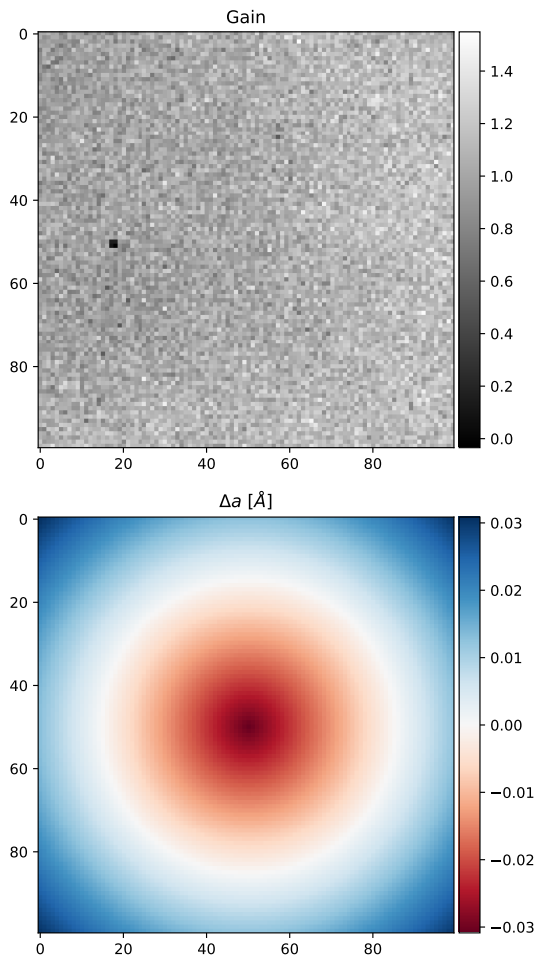
Figure 1.4 Input maps introduced when simulating the observations. The top panel represents the gain generated as white Gaussian noise, with values ranging from 0.8 to 1.2. A dust speck was introduced by creating a group of four pixels with low values of $g = 0.2$ for the gain. The bottom panel shows the spatial distribution of the defects in the etalon. The distribution follows a radial pattern starting from the center of the FoV. The defects vary from 0 % deviation to up to 5×10^{-4} %, which corresponds to a shift of 3 pm. Both possible directions for the deviations have been considered. The sign of the deviation is negative at the very center, which introduces a redshift, while it is positive at the corners, causing a shift of the profile into the blue.

1.3 Fitting algorithm

We have developed an algorithm able to extract the distribution of the etalon defects and the gain map from data taken by etalon-based instruments, which enables the correction of the two contributions separately. The algorithm works by minimizing a given merit function that depends on the gain and the etalon defects.

In particular, we have defined an error metric, ε^λ, at each tuned wavelength, computed by comparing the measured intensity with the theoretical prediction. If we let $I^{\lambda_s}_{i,\text{obs}}$ be the measured intensity at a given i pixel for an etalon tuned to the wavelength λ_s, the error metric at each wavelength is given by

$$\varepsilon^{\lambda_s}(\Delta a_i, g_i) = I^{\lambda_s}_{i,\text{obs}} - g_i \frac{\int_{\lambda_p}^{\lambda_q} O(\lambda)\Psi^{\lambda_s}(\lambda, \Delta a_i)d\lambda}{\int_{\lambda_p}^{\lambda_q} O(\lambda)\Psi^{\lambda_c}(\lambda, \Delta a_i)d\lambda}. \tag{1.13}$$

The merit function we employed is then the quadratic summation of the error metric over all tuned wavelengths:

$$f(\Delta a_i, g_i) = \sum_{s=0}^{N_\lambda} \left(\varepsilon^{\lambda_s}(\Delta a_i, g_i)\right)^2. \tag{1.14}$$

Both the camera gain and the defects of the etalon change from one pixel to another, which is why we address each pixel independently, but they remain constant at every wavelength. Hence, the transmission profile of the etalon varies at different points of the FoV; but at a given pixel, it is constant at all tuned wavelengths. Therefore, the algorithm is able to better obtain the etalon properties as we increase the number of wavelengths.

Figure 1.5 shows the derivatives of the error metric, Eq. (1.13), as a function of wavelength, that is, before computing the summation over s of the merit function, with respect to the gain, the reflectivity, and Δa. The curve corresponding to the Δa derivative is different from the others, whereas the derivatives of both the gain and the reflectivity exhibit similar shapes. Hence, variations in either the reflectivity or the gain introduce similar changes in the merit function, which can produce a trade-off between these two parameters, especially when the spectral line is sampled in only a few points. Given that discrepancies arising from errors in reflectivity are assimilated by gain maps, we did not take into account reflectivity errors when computing our simulations, as they have no impact on cavity map calculations.

A few key aspects arise when analyzing the merit function and its applicability on real data. The first point to bear in mind is that the shape of the object, $O(\lambda)$, is not known a priory. Therefore, we needed to provide a guess for it. The method works by assuming that differences between the prediction and the observation are caused exclusively by the etalon defects or the gain. If the object used during the fitting process differs considerably from the real one, the prediction and observation will have differences that will erroneously be identified as etalon defects or gain variations. This is the main source of errors for the method when applied to real data. Two approaches can be followed in order to address
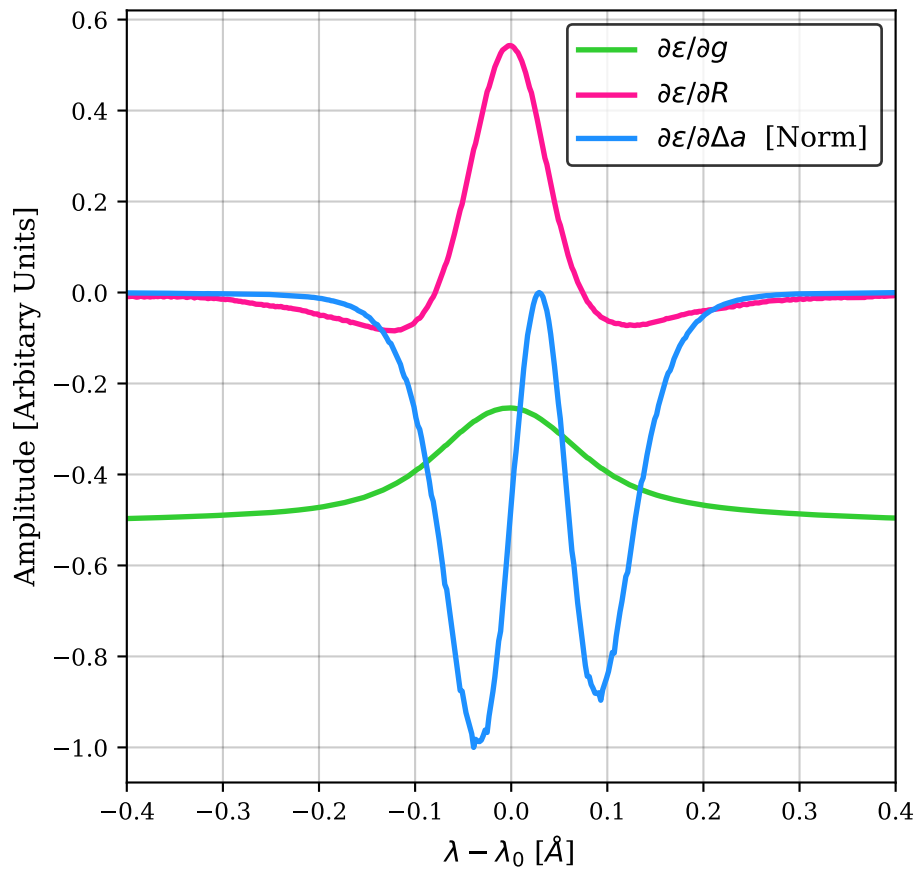
Figure 1.5 Derivatives of the error metric as a function of wavelength. The derivative with respect to Δa has been normalized in order to fit the three curves in the same plot.
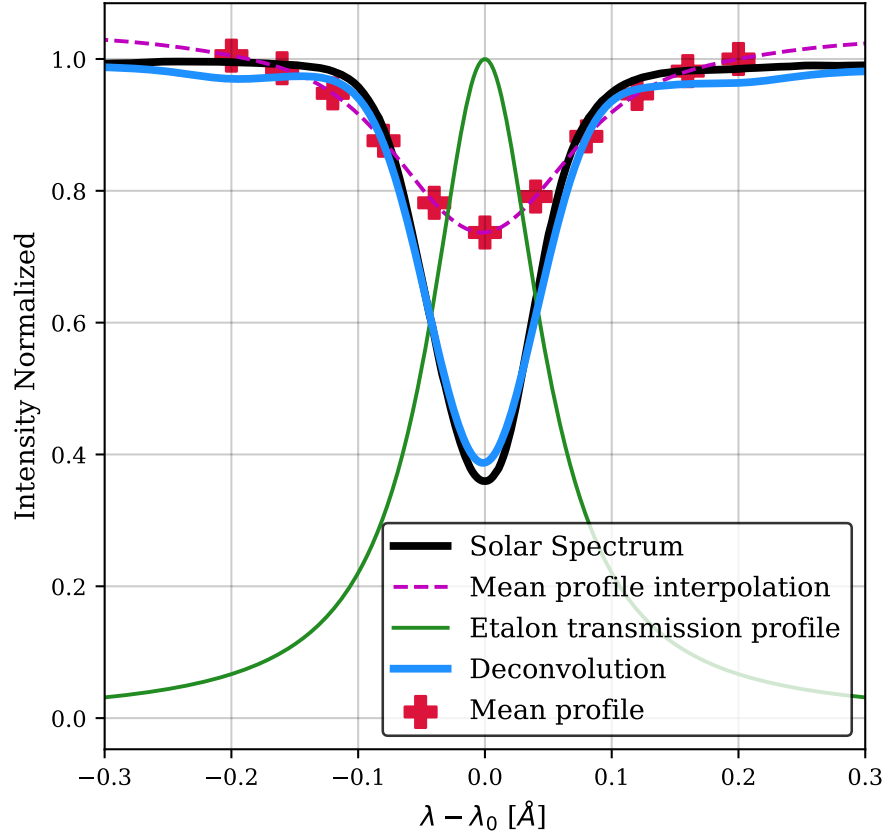
Figure 1.6 Deconvolution of the object with a measurement of the Fe I spectral line using $N_\lambda = 9$. All points of the FoV have been used to compute the average profiles (red crosses). The deconvolution (blue) is the result of deconvolving the mean profile interpolation (dashed line) with the displayed etalon transmission profile (green).

this issue. The first one consists of assuming the solar atlas profile as the object. This is a good approximation, provided the data to which the algorithm is applied to lack information about solar structure, either because they are observations of long integration times of the quiet sun or produced by averaging several quiet sun observations (flat fields). If this condition cannot be met, this approach is not valid. The second approach involves deriving an approximated object from the data themselves by deconvolving the mean profile of the observation with the etalon's transmission profile. This approach can account for any difference the real object may have with the solar atlas and thus has a greater resemblance to the real object. Nevertheless, the process of deconvolving is prone to errors when the sampling is insufficient and can introduce additional noise into the problem. We have tested both approaches to compare their performances on different scenarios in order to assess when to use one or the other.

We employed Newton's method to minimize the merit function, Eq. (1.14), as it has been proven to quickly converge (in five iterations or fewer, usually). The method begins

by assuming an initial guess for the gain g_j and Δa_j parameters. Then, provided the initial guess is sufficiently close to the solution and that the merit function is continuous and differentiable, the gain g_j and Δa_j encoded in the vector, $\mathbf{x}_j$, can be updated iteratively at each iteration, j, as

$$\mathbf{x}_{j+1} = \mathbf{x}_j - \mathcal{H}^{-1}\mathcal{J}^T f(\mathbf{x}_j) , \qquad (1.15)$$

where $\mathcal{H}$ and $\mathcal{J}$ are the Hessian and Jacobian matrices of the merit function f, respectively, calculated for $\mathbf{x}_j = [g_j, \Delta a_j]^T$, and T stands for the transpose. Hence, the transmission profile of the etalon and its derivatives have to be computed for every wavelength and every pixel at each iteration. This can be computationally costly, especially when using imperfect telecentric configurations, where numerical integrals are involved. All derivatives needed for the algorithm are calculated analytically, except when simulating imperfect telecentrism. A detailed formulation of these derivatives is provided in the appendix.

Regarding the object $O(\lambda)$, if we assume it is given by the solar atlas, no additional computations are needed. However, when using the deconvolution approach, the object has to be calculated in each iteration. In this case, the algorithm works as follows: First, we compute the average profile across the whole FoV, and we force the continuum intensity to be the same on both sides of the spectral range to reduce the boundary effects of the deconvolution. This step is only necessary in case the spectral line is sampled in only a few positions, as is the case of the SO/PHI, IMaX, or TuMag instruments, where only a continuum point, either at the red or the blue side of the spectrum, is recorded. Both the object and transmission profile require a good spectral sampling to accurately compute the integrals of Eq. (1.13). Second, a cubic spline interpolation is applied to the generated average profile to artificially improve the spectral sampling, if necessary. Finally, the interpolated profile is then deconvolved by means of a Wiener filter with the etalon's transmission profile. The result of this deconvolution is the object, $O(\lambda)$, used in the minimization algorithm. The deconvolution of the object is done every time the etalon defects are updated in order to improve the resemblance of the deconvolved object to the real one. Figure 1.6 shows an example of this process in a simulated observation using nine scanned points and a collimated configuration. The deconvolution manages to reproduce the original signal, with only some minor differences in the line core and the beginning of the wings.

1.3.1 Test scenarios and results

The aim of the simulations carried out in this section was to characterize the role of the noise $\delta_i^{\lambda_s}$, the spectral sampling, the selection of the object $O(\lambda)$, and the accuracy of the method for both the collimated and telecentric configurations. All simulations were run for different choices of the number of scanned wavelengths, ranging from $N_\lambda = 5$ to $N_\lambda = 21$.

1.3.1.1 Impact of the noise level

We first assumed that the spectrum of the observed object is given by the solar atlas. This way, all errors in the derivation of the gain and etalon defects only come from the noise

introduced into the measurement. We refer to this as the "ideal case." Since we were combining different measurements taken at different wavelengths, we considered a worst-case scenario and simulated three different signal-to-noise ratios: 100, 150, and 200.

We restricted imperfections in the telecentrism to arise only for one scenario, S/N = 200, since simulating imperfections requires a high computational effort due to the lack of a theoretical expression for both the transmission profile and its derivatives. We also assumed that the degree of telecentrism (0.3°) is known in this case.

Figure 1.7 shows the average absolute error in g (top panel) and in Δa (bottom panel) over the whole FoV as a function of the wavelength sampling, N_λ. The error in g is expressed as a percentage of its real value. Errors in Δa are given in meters per second since they are mostly responsible for shifting the profile. Errors in Δa can be translated into velocity errors with the center-of-gravity method (Uitenbroek, 2003) through the expression

$$v_{\text{los}} = \frac{c\Delta\lambda}{\lambda_s},\tag{1.16}$$

where $\Delta\lambda$ is the spectral shift of the transmission peak produced by the error in Δa.

All the scenarios exhibit a similar behavior as far as their dependence on the spectral sampling is concerned, namely, the absolute errors decrease monotonically when the wavelength sampling increases. The reason for this is simply that a larger number of wavelength samples increases the amount of available information that the algorithm can use, thus making the fitting for g and Δa more precise. These results highlight the importance of properly sampling the targeted spectral line. A modest sampling of only $N_\lambda = 5$ can produce errors as large as $120\,\text{ms}^{-1}$ in the worst-case scenario (S/N = 100).

The noise level also plays an important role in the accuracy of the results. Scenarios with a lower S/N always have larger errors, for a given N_λ, in both the gain and Δa computations. The difference in the performance of the algorithm due to the noise also changes with the spectral sampling; scenarios with a poor spectral sampling suffer from larger differences in the accuracy between the different S/N ($50\,\text{ms}^{-1}$ for $N_\lambda = 5$ between S/N = 200 and S/N = 100) than those with higher samplings ($35\,\text{ms}^{-1}$ for $N_\lambda = 21$).

The optical configuration of the etalon has a very small impact on the accuracy of the algorithm. Results for the three setups are very similar, particularly in the gain calculation, for which the results are almost identical for all configurations. Retrieval of Δa is slightly better for the collimated mount, though.

Figure 1.8 shows the spatial distribution of the errors in the retrieval of Δa for different choices of N_λ. There are no signs of a radial distribution in the maps shown in the figure, contrary to the actual distribution of the Δa parameter, as shown in Fig. ??, bottom panel. This means that the precision of the method is similar no matter the amplitude of the defects, that is, we achieve the same accuracy in the retrieval of defects associated with shifts of 3 pm ($\sim 1450\,\text{ms}^{-1}$, near the corners of our FoV), which correspond to cavity errors of around 1.5 nm or incidence angles of approximately 0.4 degrees, and in the retrieval of regions where no defect is present (radius of 20 pixels from the center of the FoV approximately). Instead of a radial distribution, the errors follow a Gaussian-like distribution (shown at the bottom panels in 1.8) similar to the one followed by the noise contribution.
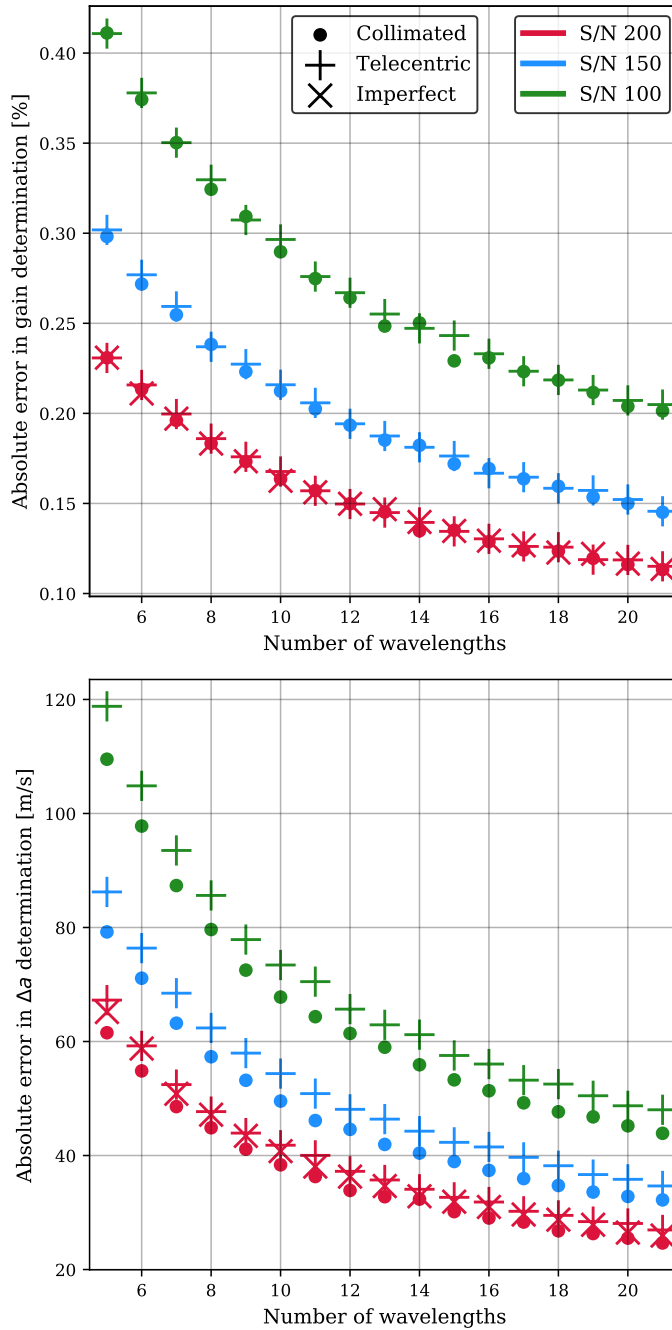
Figure 1.7 Absolute errors of the gain (top) and etalon defect (bottom) derivations averaged over all the FoV. The number of wavelengths corresponds to the parameter N_λ of wavelengths used to scan the profile.
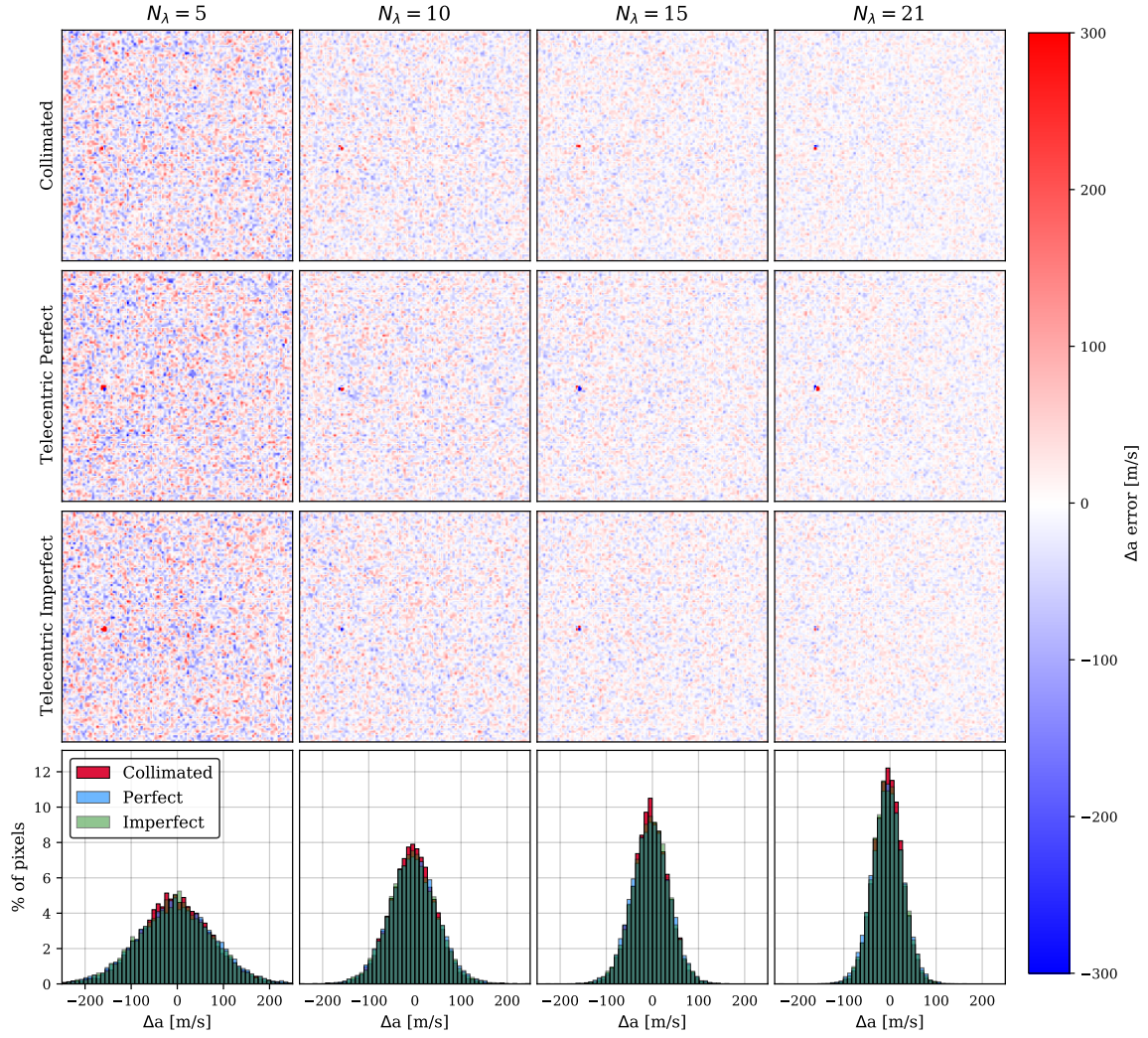
Figure 1.8 Distribution of the errors in the Δa computation for the three configurations (first three rows) and different spectral samplings (columns). In the bottom panels of each column, the error distribution for the corresponding spectral sampling is shown for the three configurations.

The standard deviation of the errors for both the gain and Δa computations are also reduced with an increase in spectral sampling. The last row of Fig. 1.8 displays the error distributions in the calculation of Δa for the three optical configurations and different spectral samplings. These results illustrate how the three configurations yield practically identical results and how the distribution narrows as N_λ increases, thereby improving the results. Specifically, the standard deviation decreases from 50 ms^{-1} for $N_\lambda = 5$ to 20 ms^{-1} for $N_\lambda = 21$. In the case of the gain determination, the standard deviation ranges between 0.2 % and 0.1% for the scenarios with the poorest and highest spectral sampling, respectively.

1.3.1.2   Impact of the object approximation

To infer the error of the algorithm when the object is unknown, we compared the performance of the ideal case, that is, when the object used to generate the observations is known, with the one achieved when deconvolving the object from the data. Only the collimated setup was simulated in order to focus exclusively on the errors introduced by the deconvolution. The data has been degraded by Gaussian noise with an S/N = 200 in both scenarios.

Figure 1.9 shows the results for the two approaches. Interestingly, the error in the gain for the deconvolution approach does not decrease with a larger number of wavelengths, unlike the ideal case. Nevertheless, the average error of the calculation is below 0.4 %, with a dispersion (1 σ) of $\pm$ 0.3 %. The deconvolution approach is prone to higher errors when deriving the gain due to the normalization of the profiles. The reason for this is two-fold. first, if the continuum is far enough from the spectral line, the normalization is strictly the integral over the transmission profile because the object is flat along the integration interval. However, this is not strictly true since the wings of the transmission profile can reach the spectral line (see Fig. **??**), hence modifying the normalization of the profile when the object changes at each iteration. Second, should the continuum intensity of the derived object vary with respect to its real value due to the deconvolution process (e.g., due to boundary effects), there will be a shift in the intensity of the whole profile induced by the normalization process. These two effects seem to dominate the accuracy on the gain determination, regardless of the chosen sampling.

For Δa, the performance of the method is slightly worse than for the ideal case when using the deconvolution approach. Unlike the gain determination, errors in the Δa derivation show a strong dependence on the spectral sampling. Differences between both approaches range from 10 ms^{-1} to 40 ms^{-1} and increase with decreasing N_λ. The sensitivity with N_λ is especially high up to $N_\lambda = 8$. A modest increase of N_λ from five to six improves the determination of $\Delta a \sim 20$ ms^{-1}, whereas at better spectral samplings, the difference between each simulation decreases more slowly, without any relevant improvement as the sampling increases. In any case, differences are all well within $\pm 1\sigma$.
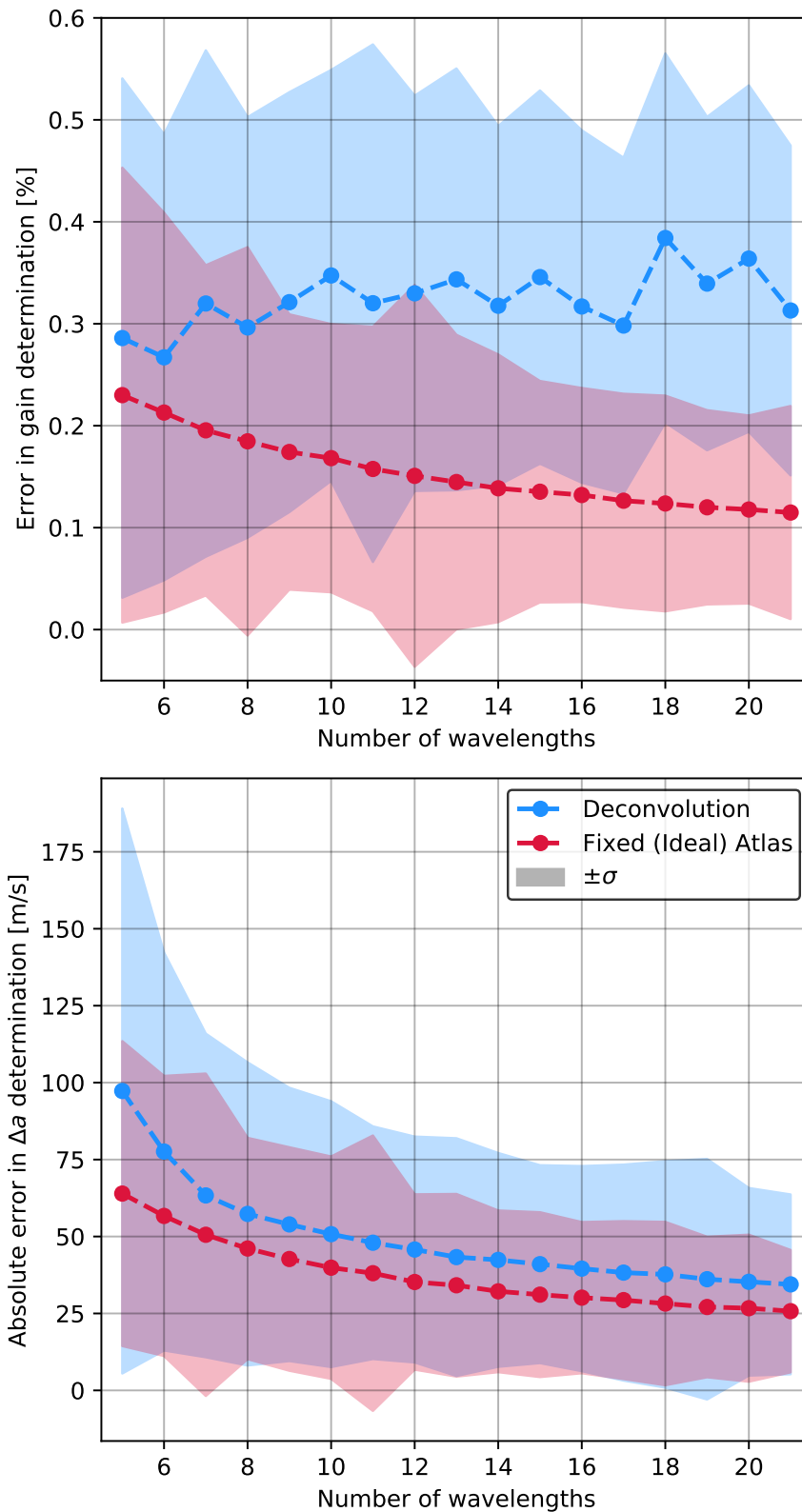
Figure 1.9 Errors in gain determination and etalon properties averaged over all the FoV with a signal-to-noise ratio of 200 and a collimated configuration.
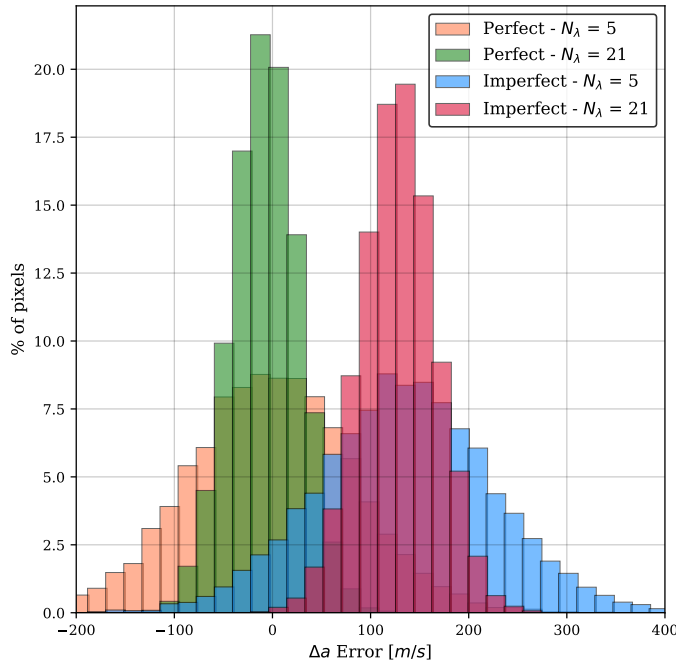
Figure 1.10 Distribution of the errors in the determination of Δa for the crossover scenarios (different configuration in the observation generation and minimization algorithm) for both perfect and imperfect configurations. Only results for the two extreme spectral samplings ($N_\lambda = 5$ and $N_\lambda = 21$) are shown.

1.3.2 The crossover case

The fact that the sensitivity of the model to the gain and to the Δa parameters are different guarantees (to some extent) that the parameters can be separated from each other. The treatment of the problem is very different between etalon configurations, and therefore full knowledge of the setup is critical. However, this is not always feasible due to the unavoidable presence of errors, misalignment, and imperfections on the instrument. Approximations to describe the optical setup are also common in the pipeline of an FPI instrument because they reduce computational efforts. For instance, telecentric mounts are usually simplified as collimated setups, as the f-numbers employed in solar instruments are usually very large. Imperfections of telecentrism are commonly neglected, too. In this section, we analyze the impact of assuming an incorrect etalon mounting. To do so, we repeated the previous exercise, starting from a perfect and imperfect telecentric configuration but assuming that the transmission profile shape corresponds to a collimated one.

In this exercise, we assumed that we have an instrument with an FPI in a telecentric mount, as in the previous sections, in both perfect and imperfect configurations and an S/N = 200. We also considered that the object is given by the spectral solar atlas. The shift of the perfect telecentric transmission profile with respect to the collimated one was corrected using Eq.52 from Bailén et al. (2019) to avoid the emergence of spurious velocity signals. Imperfections in the telecentrism shift the profile more. This additional displacement was left uncorrected intentionally so we could study its effects.

Figure 1.10 shows the error distributions for Δa when the model assumes a collimated configuration for $N_\lambda = 5$ and $N_\lambda = 21$ and for both perfect and imperfect configurations. The amplitude and dispersion of the error distributions are very similar for the two mounts

and are comparable to the results obtained in the ideal case (Fig. 1.8, bottom panel). The main difference between the perfect and imperfect scenarios is a shift of 130 ms^{-1} for the reason mentioned above. We note that this shift can easily be accounted for since it is a known and measurable effect.

The similarity in the error distributions for the calculation of Δa in the two scenarios demonstrates that the error incurred when assuming a collimated etalon does not significantly impact the determination of the cavity maps of the etalon. This is because changes in Δa mostly induce a shift of the transmission peak by an equal amount in both cases.

We note, however, that the amplitude, width, and shape of the transmission profile differ significantly between the telecentric and collimated configurations, leading to an expected higher error in gain calculation. Figure 1.11 shows the absolute errors in gain and Δa calculations for both crossover scenarios and the ideal case after correcting the wavelength shift between the different mounts. For Δ_a, the performance of the method is very similar in the three setups, as also observed earlier. This behavior is nevertheless anticipated since the properties selected for simulating the imperfect etalon were chosen to mirror those of the SO-PHI etalon, which were adjusted to closely resemble the behavior of a collimated etalon to the greatest extent possible.

The differences are larger for the gain determination. Not only are the errors higher in the crossover cases, but the trend is entirely different. Instead of decreasing when increasing the number of wavelengths, gain errors remain the same for the perfect case and increase with the number of samples for the imperfect case. Similar to the deconvolution case (Fig. 1.9), the difference between transmission profiles introduces an error in the normalization process that systematically affects the rest of the measurements. This effect becomes more pronounced as the number of wavelengths increases, given that this error is introduced more frequently, and it is even more prominent in the imperfect case, as not only are the profiles different in this scenario, but they are also asymmetric. This asymmetry results in an imbalance in the measurement of the profile, as one wing of the spectral line has a higher transmissivity and is observed with greater intensity than the other.

Our results suggest that assuming an etalon in a collimated configuration for instruments with telecentric mounts can be a good first-order approximation for cavity map calculations, provided that the level of asymmetry of the transmission profile is known. However, achieving an accurate knowledge of the degree of telecentrism is often challenging in real instruments, as it usually varies across the FoV. Meanwhile, the results highlight that this approximation leads to a considerable increase in the error in the gain determination, which increases when increasing the spectral sampling. This contrasts with the standard philosophy of solar instrumentation, which requires a high number of points to better scan the spectral line.
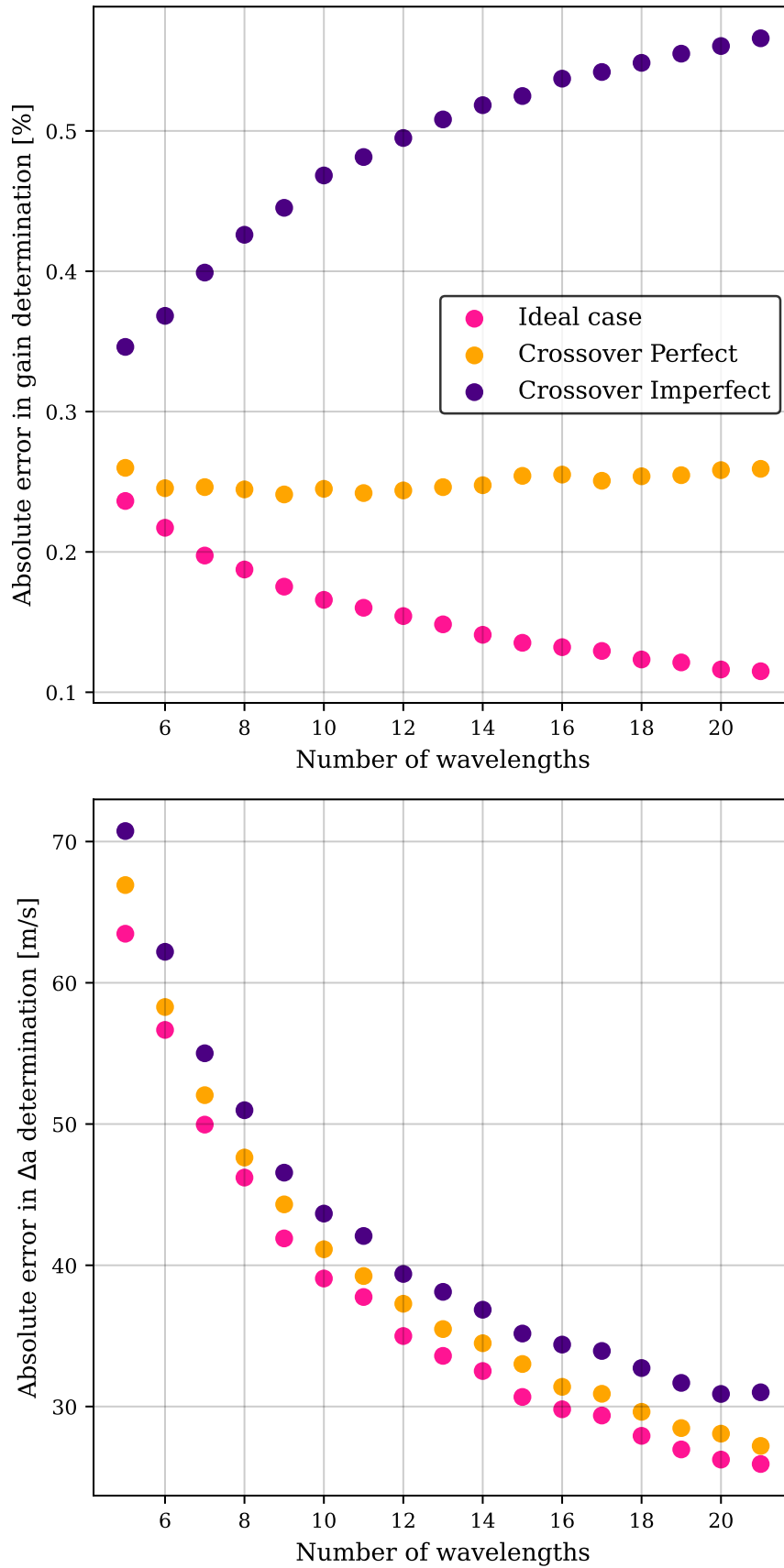
Figure 1.11 Average errors of the gain (top panel) and etalon defect (bottom panel) calculations over all the FoV for the two crossover cases and the standard case (also shown in Fig. 1.7 as the collimated case with S/N = 200) for reference. All Δa errors have been computed by correcting differential offsets of the transmission profile between the different mounts

CHAPTER 2

## SUMMARY AND CONCLUSIONS
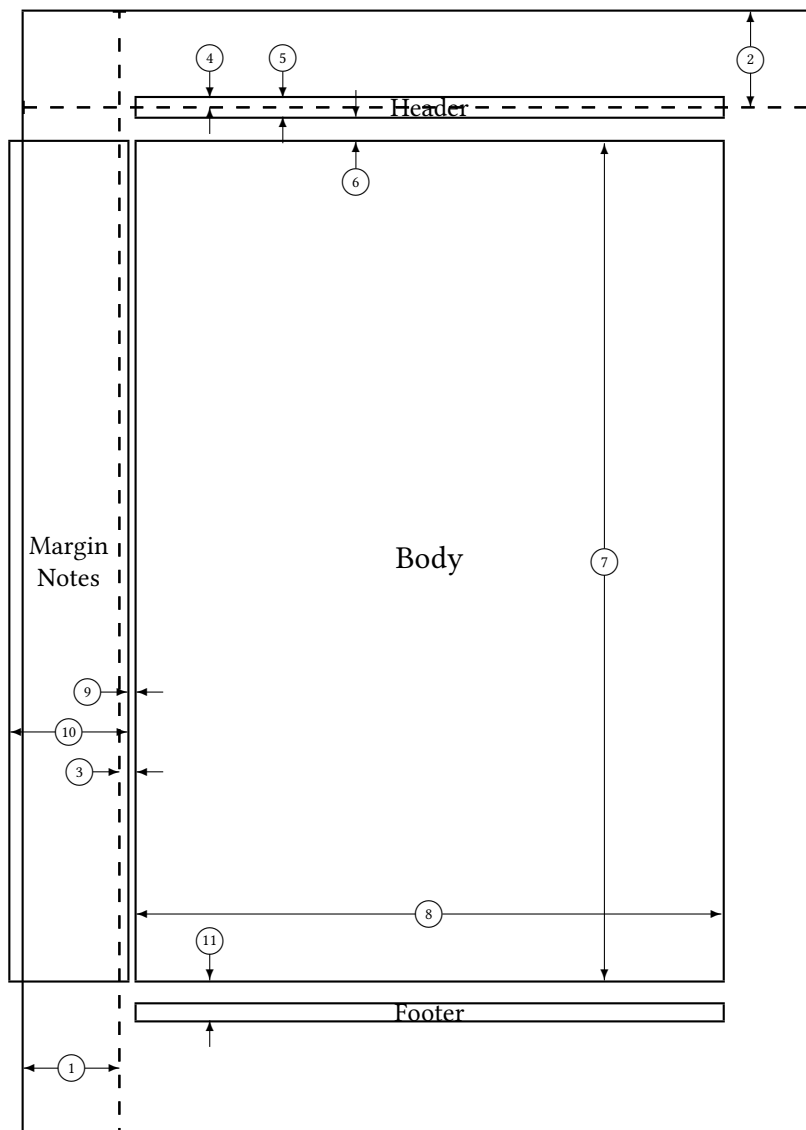
The conclusions are …

APPENDIX A

PROFILE DERIVATVIES

Bibliography

Bailén, F. J., Suárez, D. O., & del Toro Iniesta, J. On fabry–pérot etalon-based instruments. i. the isotropic case. *The Astrophysical Journal Supplement Series* **241**, 9 (2019).

Bailén, F. J., Suárez, D. O., & del Toro Iniesta, J. On fabry–pérot etalon-based instruments. iv. analytical formulation of telecentric etalons. *The Astrophysical Journal Supplement Series* **254**, 18 (2021).

Beckers, J. On the effect of narrow-band filters on the diffraction limited resolution of astronomical telescopes. *Astronomy and Astrophysics Supplement Series* **129**, 191 (1998).

Brault, J., & Neckel, H. Spectral atlas of solar absolute disk-averaged and disk-center intensity from 3290 to 12510 å. *unpublished (tape-copy from KIS IDL library)* (1987).

Scharmer, G. Comments on the optimization of high resolution fabry-pérot filtergraphs. *Astronomy & Astrophysics* **447**, 1111 (2006).

Uitenbroek, H. The accuracy of the center-of-gravity method for measuring velocity and magnetic field strength in the solar photosphere. *The Astrophysical Journal* **592**, 1225 (2003).
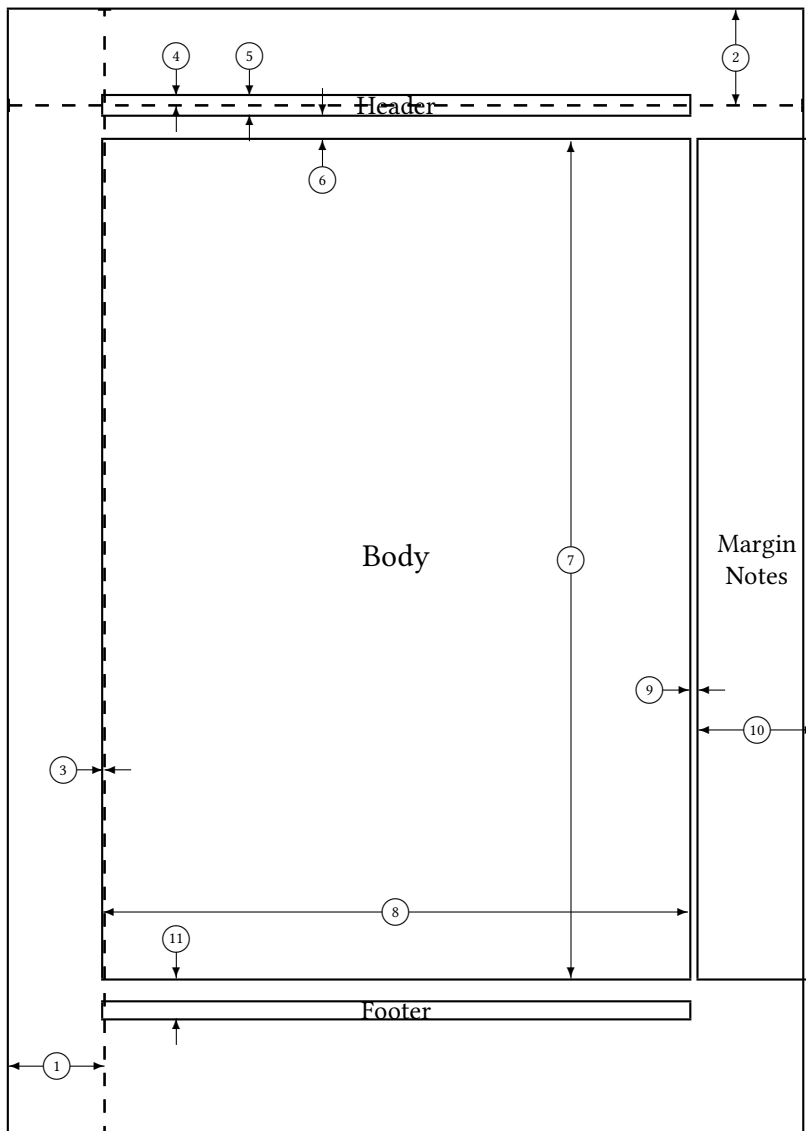
```
 1  one inch + \hoffset          2  one inch + \voffset
 3  \oddsidemargin = -1pt        4  \topmargin = -7pt
 5  \headheight = 14pt           6  \headsep = 19pt
 7  \textheight = 631pt          8  \textwidth = 441pt
 9  \marginparsep = 7pt         10  \marginparwidth = 88pt
11  \footskip = 30pt                \marginparpush = 7pt (not shown)
    \hoffset = 0pt                  \voffset = 0pt
    \paperwidth = 597pt             \paperheight = 845pt
```

Header

Body

Margin
Notes

Footer

1	one inch + \hoffset	2	one inch + \voffset
3	\evensidemargin = 13pt	4	\topmargin = -7pt
5	\headheight = 14pt	6	\headsep = 19pt
7	\textheight = 631pt	8	\textwidth = 441pt
9	\marginparsep = 7pt	10	\marginparwidth = 88pt
11	\footskip = 30pt		\marginparpush = 7pt (not shown)
	\hoffset = 0pt		\voffset = 0pt
	\paperwidth = 597pt		\paperheight = 845pt